


 Cite this: *RSC Adv.*, 2025, 15, 9153

# Preparation and electrochemical performance of an $\text{Fe}_{0.5}\text{Co}_{0.2}\text{Ni}_{0.3}\text{S}_2$ cathode material for thermal batteries

Yichun Xu, Hongliang Li, Yong Cao, Chao Wang \* and Yanhua Cui \*

Transition metal sulphides have been widely studied in the field of thermal batteries, but their low decomposition temperature, low conductivity, and discharge capacity are still pressing issues hampering their practical application. Inspired by the strategy of entropy increase in sodium-ion and lithium-ion batteries, herein, we propose an  $\text{Fe}_{0.5}\text{Co}_{0.2}\text{Ni}_{0.3}\text{S}_2$  cathode material possessing the advantages of electrochemically active elements Fe, Co, and Ni.  $\text{Fe}_{0.5}\text{Co}_{0.2}\text{Ni}_{0.3}\text{S}_2$  exhibited a thermal decomposition temperature of 591 °C, which was significantly higher than that of  $\text{FeS}_2$ . Furthermore, the wettability of the LiCl–KCl molten salt on the surface of  $\text{Fe}_{0.5}\text{Co}_{0.2}\text{Ni}_{0.3}\text{S}_2$  was improved and its contact area was 1.1 times that of  $\text{FeS}_2$ , providing more active sites for electrochemical reactions and effectively improving the electrochemical performance of the material. Moreover, it exhibited a specific capacity (cutoff voltage  $\geq 1.5$  V) of 584 mA h  $\text{g}^{-1}$  at 500 °C with a discharge current of 100 mA  $\text{cm}^{-2}$ , representing an increase of approximately 96.5% compared to that of  $\text{CoS}_2$ . Thus, this work presents a new strategy for the design of high-performance cathode materials for thermal batteries.

Received 14th January 2025

Accepted 6th March 2025

DOI: 10.1039/d5ra00351b

[rsc.li/rsc-advances](https://rsc.li/rsc-advances)

## 1. Introduction

Thermal batteries have made a significant contribution to the development of military equipment, and their discharge performance is largely influenced by their cathode materials, with transition metal sulfides  $\text{MS}_2$  ( $\text{M} = \text{Fe}, \text{Co}, \text{and Ni}$ ) being the most widely used.<sup>1–6</sup> Among them,  $\text{FeS}_2$  is a cost-effective option that offers a high lithium potential (2.1 V) and a high theoretical specific capacity of the first discharge platform (335 mA h  $\text{g}^{-1}$ ). However, it has lower thermal stability (thermal decomposition temperature of 550 °C) and high resistivity (0.036  $\Omega$  cm).<sup>2</sup> Although  $\text{CoS}_2$  has better thermal stability (thermal decomposition temperature of 650 °C) and resistivity (0.002  $\Omega$  cm), it is relatively expensive and has a lower lithium potential (2.0 V) and lower theoretical specific capacity (290 mA h  $\text{g}^{-1}$ ) in the first discharge platform.<sup>3,7,8</sup>  $\text{NiS}_2$  has a high theoretical specific capacity of the first discharge plateau (437 mA h  $\text{g}^{-1}$ ), and its thermal stability and conductivity are in between  $\text{FeS}_2$  and  $\text{CoS}_2$ . However, it has a lower potential for lithium (2.0 V) and a discharge product with lower conductivity.<sup>3</sup> Although monometallic sulfides have their own advantages and disadvantages, the ongoing replacement of current weapon systems necessitates even higher and more comprehensive requirements for cathode materials in thermal batteries. Therefore, the development of cathode materials with

superior thermal stability and electrochemical properties is necessary.

Previous studies have demonstrated that entropy increase is a promising strategy to address the intrinsic limitations of battery materials. This strategy involves designing materials with multiple components and changing the types of elements to create more combinations of potential interactions, which ultimately stabilize the crystal structure and significantly enhance the performance of the electrode materials.<sup>9–12</sup> In cathode materials, due to the diffusion retardation effect of the entropy increasing strategy, layered transition metal oxides, polyanionic compounds, and Prussian blue analogues can inhibit the deleterious phase evolution during electrochemical processes and thus enhance their electrochemical performance.<sup>10,13</sup> For example, Pei *et al.*<sup>14</sup> prepared a medium-entropy cathode material,  $\text{Li}_{1.46}\text{Ni}_{0.32}\text{Mn}_{1.2}\text{O}_{4-x}$  ( $0 < x < 4$ ), using this strategy, which improved the structural stability and discharge capacity of the cathode material by altering its lithium-ion storage mechanism through the medium-entropy state generated by partial cation disorder and bypassing the symmetry changes inherent in the conventional spinel phase. Ding *et al.*<sup>15</sup> designed a nickel-rich oxide cathode material (Ni-rich oxide cathode) that is capable of controlling the structural changes and increasing the electrode operating potential, thereby improving the performance of sodium-ion batteries. In addition, in metal oxide anodes, the “cocktail effect” of multi-element components can be attributed to the transformation of the initial structure into a stable self-assembled structure during cycling, which promotes the faster conduction of

*Institute of Electronic Engineering, China Academy of Engineering Physics, Mianyang 621900, P.R.China. E-mail: cuiyanhua@netease.com; wangchao\_1988924@126.com*



electrons and ions. In the case of solid-state electrolytes, the lattice distortion effect can alter the potential energy of alkali ions and promote the generation of diffusion networks, thereby enhancing their ionic conductivity.

This strategy has been extensively applied in sodium-ion and lithium-ion batteries, allowing us to gain valuable experience from existing reports to guide the design of cathode materials for thermal batteries. In this work, we utilized a high-temperature sintering technique to develop a ternary metal sulfide cathode,  $\text{Fe}_{0.5}\text{Co}_{0.2}\text{Ni}_{0.3}\text{S}_2$ , focusing on improving its thermal stability and specific capacity. This material showed excellent properties by combining the advantages of the Fe, Co, and Ni electrochemically active elements. The comparative analysis with conventional sulfide cathodes revealed that  $\text{Fe}_{0.5}\text{Co}_{0.2}\text{Ni}_{0.3}\text{S}_2$  exhibited superior thermal stability, reduced contact angle, and optimized electrochemical characteristics. Its enhanced thermal stability ensures the high utilization efficiency of electrode materials, which in turn extends the lifespan of the battery. Meanwhile, the optimized electrochemical properties enhanced the battery efficiency by improving the conductivity and mitigating the energy loss. These optimized attributes position this ternary sulfide as a promising cathode candidate for energy storage applications and provide valuable insights for the design of thermal batteries that require high capacity and extended operational lifespan.

## 2. Experimental

### 2.1 Material preparation

The raw materials used in this study were acquired from commercial suppliers and of high analytical purity. Firstly, 1.2 g of sublimated sulfur powder with 99.8% purity and 0.6 g of FeCoNi alloy powder were weighed. Subsequently, the powders were combined in an onyx mortar and ground for 15 to 20 min. After grinding, the mixture was poured into a crucible and heated to 500 °C in flowing argon gas at a rate of 10 °C per min, and then heated in a tube furnace for 4 h. Finally, desulfurization was carried out at 400 °C for 4 h to remove the excess sulfur during the experiment (Fig. 1).

### 2.2 Material characterization

The physical structure and chemical composition of the prepared materials were characterized using powder X-ray

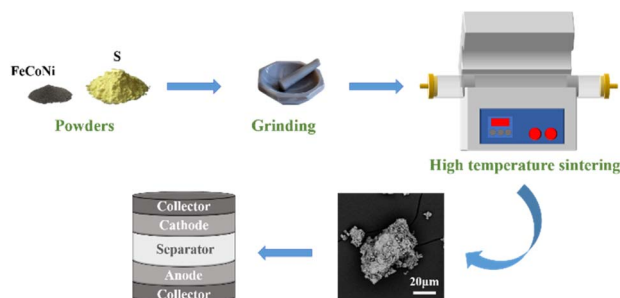


Fig. 1 Schematic of the preparation process and single cell structure of trimetallic sulfide  $\text{Fe}_{0.5}\text{Co}_{0.2}\text{Ni}_{0.3}\text{S}_2$ .

diffraction (XRD, Bruker D8 Advance, Cu-K $\alpha$  radiation,  $\lambda = 1.5406 \text{ \AA}$ ) in the  $2\theta$  diffraction angle range of 20–80°. Its elemental composition was analyzed *via* ICP-OES (Agilent 5110(OES)). The emission lines of Fe (238.204 nm), Co (238.892 nm), Ni (231.604 nm), and S (181.972 nm) were selected as analytical lines. The sample solution was prepared by soaking in aqua regia (HCl :  $\text{HNO}_3 = 1 : 1$ ) for 2 h, followed by microwave digestion with HF. The digested solutions were evaporated to near dryness and  $\text{HNO}_3$  added, and then diluted to 50 mL with ultrapure water. Complete digestion was confirmed by examining the clarity and transparency of the solution, which is critical for ensuring analytical accuracy. The calibration curves were constructed using six-point standards for Fe, five-point standards for Co and Ni, and four-point standards for S. Thermal stability was analyzed using a simultaneous thermal analysis system (TG-DSC, STA449 F3) with an argon atmosphere, at a heating rate of 10 °C per min and a temperature range of 30–800 °C. The morphology and elemental distribution of the samples were observed using scanning electron microscopy (SEM, Phenom Prox, and ZEISS Sigma 360), coupled with energy spectroscopy analysis (EDS). The specific surface area was measured with a fully automated specific surface technology porosity analyzer (BET, Quantachrome Nova 4000e). The contact angle test system (TC700pro, Data physics) was used to evaluate the wettability of the solid surfaces. This system was first heated to the desired temperature (500 °C), and 15 mg of LiCl–KCl molten salt electrolyte particles were placed on the electrode substrate in a glove box in an inert atmosphere, and the contact angle between the sample and the electrode substrate was determined by waiting for the molten salt electrolyte to melt.

### 2.3 Assembly of single cells

All the electrode material pre-treatment and cell assembly processes were carried out in a controlled drying environment, with a dew point maintained at less than  $-50 \text{ }^\circ\text{C}$ . In the case of the anode in the single cell, a 32 mm diameter Li–B alloy was used, containing 55 wt% Li. The electrolyte separator was composed of a powder mixture consisting of 55 wt% MgO and 45 wt% (LiCl–KCl). The cathode used consisted of a mass fraction of 80% active substance mixed with 20% electrolyte milling. The single cells were assembled using a layered pressing technique in a mold with a diameter of 32 mm and subjected to a pressure of 150 MPa, followed by demoulding to obtain the final cells.

### 2.4 Electrochemical measurement

The batteries underwent constant current discharge testing using an Arbin BT-ML battery testing system, with constant current discharge current densities of 100, 300, 500, and 1000  $\text{mA cm}^{-2}$ , at a test temperature of 500 °C, with a cut-off voltage of 0 V. The pulse tests were carried out with pulse current densities of 300 and 1000  $\text{mA cm}^{-2}$  for 1 s at 500 °C. The steady current density was 100  $\text{mA cm}^{-2}$  for 30 s. All electrochemical performance tests for the single cells in this study were conducted in a glove box under an argon atmosphere.



### 3. Results and discussion

#### 3.1 Microstructure features of the synthesized samples

The phase structure of the materials was characterized by XRD, as shown in Fig. 2. All the characteristic peaks of  $\text{Fe}_{0.5}\text{Co}_{0.2}\text{Ni}_{0.3}\text{S}_2$  correspond well to the face-centered structures of  $\text{FeS}_2$  (PDF#97-000-0316),  $\text{NiS}_2$  (PDF#04-004-3801) and  $\text{CoS}_2$  (PDF#97-005-6017), with no additional diffraction peaks detected. This indicates that the samples have high purity. Notably, compared with the positions of the (200) and (311) peaks of the three sulfides, shifts in the diffraction peaks were observed in the final sample. Despite these shifts, the peak intensities and overall lattice positions remained consistent. This phenomenon is likely attributed to the different ionic radii of  $\text{Fe}^{3+}$ ,  $\text{Ni}^{2+}$ , and  $\text{Co}^{2+}$ , which affect the spacing of the crystal planes when bonding with  $\text{S}^{2-}$ .<sup>16–18</sup> To gain further insights into the crystal structure of  $\text{Fe}_{0.5}\text{Co}_{0.2}\text{Ni}_{0.3}\text{S}_2$ , Rietveld refinement was performed on the XRD data. The results indicate that  $\text{Fe}_{0.5}\text{Co}_{0.2}\text{Ni}_{0.3}\text{S}_2$  belongs to the cubic crystal system with the space group  $Pa\bar{3}$  (205), exhibiting a structure similar to  $\text{FeS}_2$ ,  $\text{CoS}_2$ , and  $\text{NiS}_2$ . The refined lattice constants for  $\text{Fe}_{0.5}\text{Co}_{0.2}\text{Ni}_{0.3}\text{S}_2$  are  $a = b = c = 5.595735 \text{ \AA}$ , with  $\alpha = \beta = \gamma = 90^\circ$ . Additionally, the low  $R_{\text{wp}}$  value

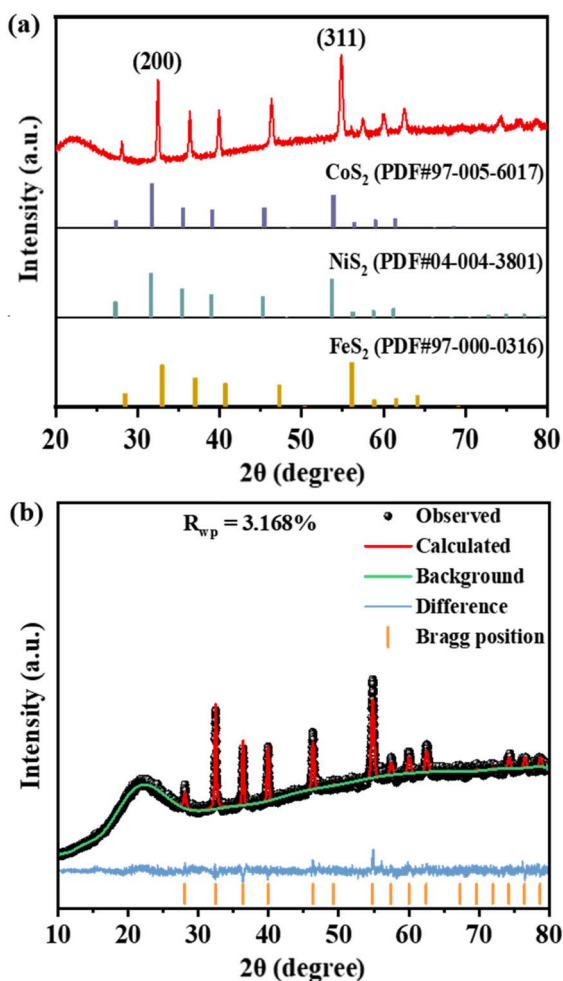


Fig. 2 (a) XRD patterns of  $\text{FeS}_2$ ,  $\text{NiS}_2$ ,  $\text{CoS}_2$  and  $\text{Fe}_{0.5}\text{Co}_{0.2}\text{Ni}_{0.3}\text{S}_2$ . (b) XRD Rietveld refinement.

Table 1 ICP test results for sample 1

Sample quality (g)	Test element	Sample element content (%)
0.05053	Fe	25.76
0.05053	Co	8.25
0.05053	Ni	15.26
0.05053	S	51.11

Table 2 ICP test results for sample 2

Sample quality (g)	Test element	Sample element content (%)
0.05053	Fe	25.80
0.05053	Co	8.24
0.05053	Ni	15.23
0.05053	S	51.13

of 3.168% obtained by Rietveld refinement indicates a good fit between the experiment and the simulation. ICP (inductively coupled plasma optical emission spectroscopy) was used to further determine the elemental content of the samples twice, and the results are shown in Tables 1 and 2. The correlation coefficients of the calibration curves for all elements were  $\geq 0.999$ . This demonstrates the robust linear relationship between the analyte concentration and signal intensity, confirming the reliability of the test results. Further calculations indicated that the molar ratio of Fe, Co, and Ni atoms in the material is approximately 5 : 2 : 3.

The SEM and mapping images of the  $\text{Fe}_{0.5}\text{Co}_{0.2}\text{Ni}_{0.3}\text{S}_2$  sample prepared by high-temperature sintering are shown in Fig. 3. In Fig. 3a, it can be observed that the synthesized ternary sulfide sample consists of particles with irregular shapes, which have an average size of approximately  $30 \mu\text{m}$ . The higher-magnification SEM images (Fig. 3f and g) reveal that these micrometer-scale particles are formed through the agglomeration of numerous nanoparticles. The elemental distribution diagram shows that the four elements, S, Fe, Co, and Ni, are uniformly distributed and almost completely overlapped, further confirming that the synthesized material is a single-phase Fe–Co–Ni ternary sulfide. In this work, it can be judged that the high-purity  $\text{Fe}_{0.5}\text{Co}_{0.2}\text{Ni}_{0.3}\text{S}_2$  cathode material with uniformly dispersed elements was successfully synthesized.

The  $\text{N}_2$  adsorption–desorption curve of the sample, as presented in Fig. 4, corresponds to a type IV isotherm, with an average pore diameter of 20.53 nm. In addition, the specific surface area of  $\text{Fe}_{0.5}\text{Co}_{0.2}\text{Ni}_{0.3}\text{S}_2$  obtained from the BET test is approximately  $1.57 \text{ m}^2 \text{ g}^{-1}$ , which is higher than that in the previous study.<sup>19</sup> This enhanced specific surface area contributes to improving the kinetic performance of the electrode by providing more active sites.<sup>18,20,21</sup>

Fig. 5 exhibits the TG-DSC curves of  $\text{Fe}_{0.5}\text{Co}_{0.2}\text{Ni}_{0.3}\text{S}_2$ . The sample started to decompose at about  $591^\circ\text{C}$ . Compared with  $\text{FeS}_2$  ( $550^\circ\text{C}$ ),<sup>2</sup> the thermal stability of  $\text{Fe}_{0.5}\text{Co}_{0.2}\text{Ni}_{0.3}\text{S}_2$  is significantly improved. The DSC curve displays an obvious



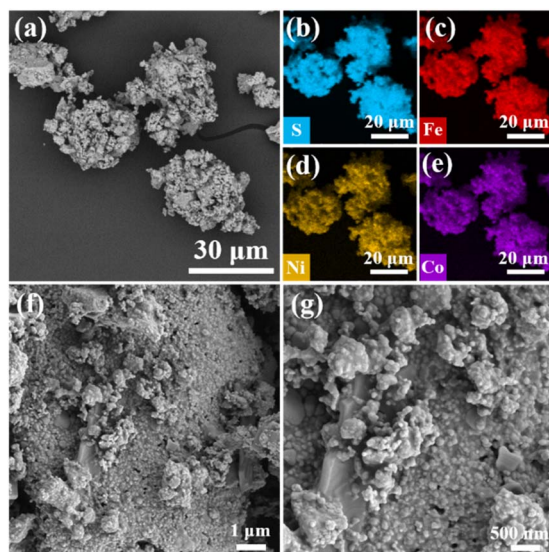


Fig. 3 (a–g) SEM images of  $\text{Fe}_{0.5}\text{Co}_{0.2}\text{Ni}_{0.3}\text{S}_2$  and corresponding EDS elemental mapping.

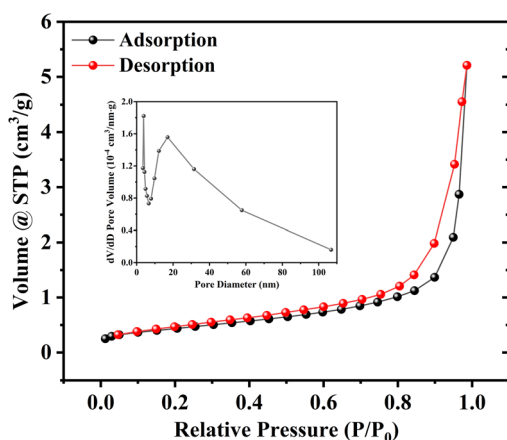


Fig. 4 Adsorption–desorption curve of  $\text{Fe}_{0.5}\text{Co}_{0.2}\text{Ni}_{0.3}\text{S}_2$ .

endothermic peak, which corresponds with the mass loss observed in the TG curve, suggesting the potential endothermic decomposition of the material at this temperature range. The peak temperature of the DSC endothermic peak ( $643.1\text{ }^\circ\text{C}$ ) closely aligns with the decomposition termination temperature ( $647.3\text{ }^\circ\text{C}$ ) observed in the TG analysis, indicating the completion of the endothermic decomposition process.

The contact angle can describe the wettability of the electrolyte to the electrode material, and according to Young's equation, the smaller the contact angle, the better the electrolyte wettability on the electrode surface.<sup>22</sup> The contact angles of the LiCl–KCl molten salt electrolyte on  $\text{Fe}_{0.5}\text{Co}_{0.2}\text{Ni}_{0.3}\text{S}_2$ ,  $\text{Fe}_{0.5}\text{Co}_{0.5}\text{S}_2$ ,  $\text{CoS}_2$  and  $\text{FeS}_2$  substrates were measured at  $500\text{ }^\circ\text{C}$ , and found to be  $114.1^\circ$  (Fig. 6b),  $127.9^\circ$  (Fig. 6c),  $124.6^\circ$  (Fig. 6d), and  $131.9^\circ$  (Fig. 6e), respectively. Among them,  $\text{Fe}_{0.5}\text{Co}_{0.2}\text{Ni}_{0.3}\text{S}_2$  has the smallest contact angle and almost 1.1 times the contact area of  $\text{FeS}_2$ , and the test results show that it has optimal

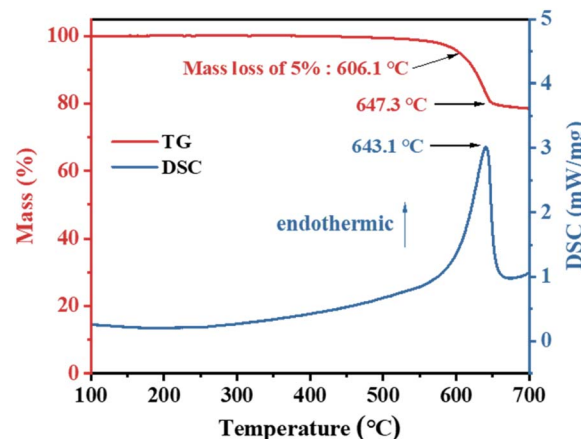


Fig. 5 Thermal stability analysis (TG–DSC curves) of  $\text{Fe}_{0.5}\text{Co}_{0.2}\text{Ni}_{0.3}\text{S}_2$ .

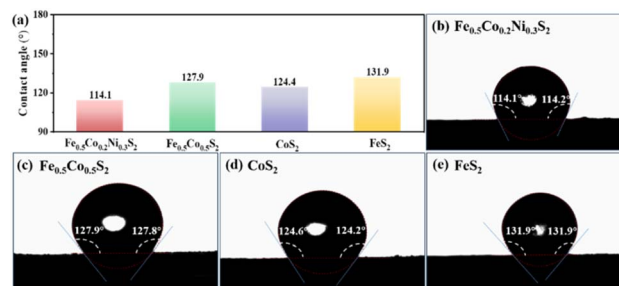


Fig. 6 (a) Columnar comparison of the contact angle of LiCl–KCl electrolyte droplets with four sulphides, and the contact angles between a LiCl–KCl droplet and the four tested sulphides at  $500\text{ }^\circ\text{C}$ : (b)  $\text{Fe}_{0.5}\text{Co}_{0.2}\text{Ni}_{0.3}\text{S}_2$ , (c)  $\text{Fe}_{0.5}\text{Co}_{0.5}\text{S}_2$ , (d)  $\text{CoS}_2$ , and (e)  $\text{FeS}_2$ .

wettability with LiCl–KCl molten salt electrolyte. The strong wettability of the molten salt electrolyte on the electrode increases the surface area available for electrochemical reactions. This larger contact area facilitates the creation of more active sites for ion and electron exchange at the interface between the electrode and electrolyte.<sup>19,23,24</sup> As a result, the interfacial contact resistance is reduced, which in turn improves the overall electrochemical performance of the material.

### 3.2 Electrochemical performance of $\text{Fe}_{0.5}\text{Co}_{0.2}\text{Ni}_{0.3}\text{S}_2$

Fig. 7a–c show the discharge curves of the single cell at various current densities and  $500\text{ }^\circ\text{C}$ . Under a discharge current density of  $100\text{ mA cm}^{-2}$ , the single cell exhibited three distinct and stable discharge platforms at  $2.04\text{ V}$ ,  $1.82\text{ V}$ , and  $1.64\text{ V}$ , demonstrating that this material can provide high precision voltage during operation. As the discharge current density increased to  $300\text{ mA cm}^{-2}$ , the voltage plateau decreased by approximately  $0.06\text{ V}$ . At a higher current density of  $1000\text{ mA cm}^{-2}$ , the discharge curve was smooth, with no distinct plateau observed. Meanwhile, as shown in Fig. 7b and c, the curves obtained from repeated tests at  $100\text{ mA cm}^{-2}$  and  $300\text{ mA cm}^{-2}$  demonstrate excellent overlap, indicating that the prepared materials possess good repeatability. At a cut-off voltage of  $\geq 1.5\text{ V}$ , it delivered specific



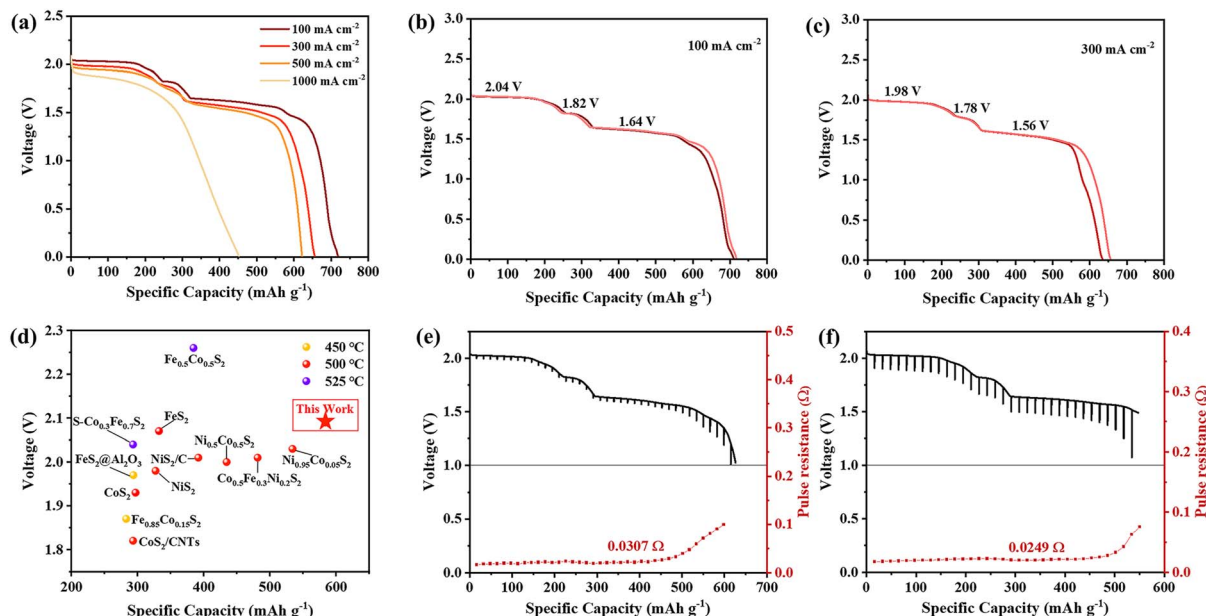


Fig. 7 (a) Electrical properties of  $\text{Fe}_{0.5}\text{Co}_{0.2}\text{Ni}_{0.3}\text{S}_2$  discharged at  $500\text{ }^\circ\text{C}$  at current densities of 100, 300, 500 and  $1000\text{ mA cm}^{-2}$ . (b) Repeat test curves at a current density of  $100\text{ mA cm}^{-2}$ . (c) Repeat test curves at a current density of  $300\text{ mA cm}^{-2}$ . (d) Comparison of sulphide cathode discharge performance.<sup>17,25–32</sup> Discharge curves and polarisation resistance of  $\text{Fe}_{0.5}\text{Co}_{0.2}\text{Ni}_{0.3}$  discharged at  $500\text{ }^\circ\text{C}$  with (e) 30 s steady current density ( $100\text{ mA cm}^{-2}$ ) and 1 s pulsed current density ( $300\text{ mA cm}^{-2}$ ) and (f) 30 s steady current density ( $100\text{ mA cm}^{-2}$ ) and 1 s pulsed current density ( $1\text{ A cm}^{-2}$ ).

capacities of  $584\text{ mA h g}^{-1}$ ,  $512.9\text{ mA h g}^{-1}$ , and  $457\text{ mA h g}^{-1}$  at current densities of 100, 300, and  $500\text{ mA cm}^{-2}$ , respectively. When the cut-off voltage increased to  $\geq 1.7\text{ V}$ , the specific capacities of the material at current densities of 100, 300, and  $500\text{ mA cm}^{-2}$  were  $310\text{ mA h g}^{-1}$ ,  $291\text{ mA h g}^{-1}$ , and  $285\text{ mA h g}^{-1}$ , respectively. Notably, this minimal variation in capacity across different current densities ( $10\text{--}500\text{ mA cm}^{-2}$ ) demonstrates the exceptional rate capability of  $\text{Fe}_{0.5}\text{Co}_{0.2}\text{Ni}_{0.3}\text{S}_2$ . Fig. 7d compares the discharge capacities of different sulfide cathode materials at a discharge capacity of  $100\text{ mA cm}^{-2}$  with an open-circuit voltage and a cut-off voltage of  $1.5\text{ V}$ .<sup>17,25–32</sup> Among them,  $\text{Fe}_{0.5}\text{Co}_{0.2}\text{Ni}_{0.3}\text{S}_2$  exhibited a superior electrochemical performance, as can be seen from the increase in open-circuit voltage and discharge specific capacity.

Polarisation resistance, which includes electrochemical polarisation, concentration polarization, and ohmic polarisation, significantly influences the discharge characteristics of sulfides. The pulse tests were performed at  $500\text{ }^\circ\text{C}$  and the discharge stability and polarisation resistance of the material obtained are shown in Fig. 7. As shown in Fig. 7e, discharge was performed at a 30 s steady current density ( $100\text{ mA cm}^{-2}$ ) and 1 s pulsed current density ( $300\text{ mA cm}^{-2}$ ) for 37 times. Fig. 7f shows the curves for the material discharged at 30 s steady current density ( $100\text{ mA cm}^{-2}$ ) and 1 s pulsed current density ( $1\text{ A cm}^{-2}$ ) for 35 times. The polarised internal resistance of a single cell under the corresponding conditions was calculated separately using the following equation:

$$R = \frac{\Delta U}{\Delta I}$$

where  $R$  is the total polarisation,  $\Delta U$  is the voltage drop induced by the pulse current, and  $\Delta I$  is the difference between the constant current and the pulse current.<sup>1,33,34</sup> It can be observed that the battery maintained a relatively stable discharge plateau and polarisation resistance during pulse discharge, and the polarisation internal resistance increased sharply when the third discharge plateau ended. The magnitude of the average polarisation resistance was calculated based on the polarisation resistance curves, which was  $0.0307\ \Omega$  for a pulse current density of  $300\text{ mA cm}^{-2}$  and  $0.0249\ \Omega$  for  $1000\text{ mA cm}^{-2}$ . Compared with the results in a previous study, the discharge performance of this material shows notable improvements in pulse behavior. This enhancement can be attributed to the increased wettability of the electrode, which leads to a larger contact area between the electrode and the electrolyte. As a result, the ion and electron exchange at the electrode/electrolyte interface is improved, interfacial impedance is minimized, and the overall discharge stability is enhanced.<sup>19,26,35</sup>

## 4. Conclusions

A novel ternary metal sulfide  $\text{Fe}_{0.5}\text{Co}_{0.2}\text{Ni}_{0.3}\text{S}_2$  cathode material was prepared using high-temperature sintering. The test results showed that this material has enhanced thermal stability and excellent wettability with LiCl–KCl molten salt electrolyte. It also exhibited a good electrochemical performance, with a specific capacity of approximately  $584\text{ mA h g}^{-1}$  at a discharge capacity of  $100\text{ mA cm}^{-2}$  (cut-off voltage of  $1.5\text{ V}$ ), which is better than that of the commonly used sulfide cathode materials.



Meanwhile, this material showed an improved pulse performance, reduced discharge polarization, and enhanced discharge stability. As a result, the  $\text{Fe}_{0.5}\text{Co}_{0.2}\text{Ni}_{0.3}\text{S}_2$  cathode material shows potential for application in thermal batteries, providing a stable discharge performance, high specific capacity, high power, and long-term durability.

## Data availability

The data supporting this article have been included within the manuscript.

## Author contributions

Yichun Xu: data curation, formal analysis, investigation, writing – original draft, review & editing. Hongliang Li: formal analysis, writing – original draft. Yong Cao: supervision. Chao Wang: supervision, project administration. Yanhua Cui: supervision, project administration, funding acquisition.

## Conflicts of interest

There are no conflicts to declare.

## Acknowledgements

This work is financially supported by the National Natural Science Foundation of China (Grant No. 52474335 and Grant No. 52377217).

## Notes and references

- R. A. Guidotti and P. Masset, *J. Power Sources*, 2006, **161**, 1443–1449.
- P. J. Masset and R. A. Guidotti, *J. Power Sources*, 2008, **177**, 595–609.
- P. J. Masset and R. A. Guidotti, *J. Power Sources*, 2008, **178**, 456–466.
- Y. Chu, S. Li, F. Chen, Y. Feng, B. Shi, L. Zhao, X. Wang and Y. Zhu, *Mater. Lett.*, 2022, **323**, 132503.
- J. Ko, S. H. Kang, H.-W. Cheong, Y. S. Yoon, J. Ko, S. H. Kang, H.-W. Cheong and Y. Yoon, *J. Korean Ceram. Soc.*, 2019, **56**, 233–255.
- J. Shin, H. Kang, Y. Lee, S. H. Ha and E. Cho, *RSC Adv.*, 2022, **12**, 4795–4804.
- J. L. Payne, J. D. Percival, K. Giagloglou, C. J. Crouch, G. M. Carins, R. I. Smith, R. K. B. Gover and J. T. S. Irvine, *J. Electrochem. Soc.*, 2019, **166**, A2660–A2664.
- Y. Xie, Z. Liu, H. Ning, H. Huang and L. Chen, *RSC Adv.*, 2018, **8**, 7173–7178.
- M. Li, C. Sun, X. Yuan, Y. Li, Y. Yuan, H. Jin, J. Lu and Y. Zhao, *Adv. Funct. Mater.*, 2024, **34**, 2314019.
- W. Zheng, G. Liang, Q. Liu, J. Li, J. A. Yuwono, S. Zhang, V. K. Peterson and Z. Guo, *Joule*, 2023, **7**, 2732–2748.
- Y. Zhao, X. Gao, H. Gao, H. Jin and J. B. Goodenough, *Adv. Funct. Mater.*, 2020, **30**, 1908680.
- X. Pang, H. Geng, S. Dong, B. An, S. Zheng and B. Wang, *Small*, 2023, **19**, 2205525.
- N. G. Garcia, J. M. Gonçalves, C. Real, B. Freitas, J. G. Ruiz-Montoya and H. Zanin, *Energy Storage Mater.*, 2024, **67**, 103213.
- Y. Pei, Q. Chen, M. Wang, P. Zhang, Q. Ren, J. Qin, P. Xiao, L. Song, Y. Chen, W. Yin, X. Tong, L. Zhen, P. Wang and C.-Y. Xu, *Nat. Commun.*, 2022, **13**, 6158.
- F. Ding, C. Zhao, D. Zhou, Q. Meng, D. Xiao, Q. Zhang, Y. Niu, Y. Li, X. Rong and Y. Lu, *Energy Storage Mater.*, 2020, **30**, 420–430.
- Y. He, L. Cao, G. Yuan, S. Fan, Q. Li, S. Bi, C. Luo and H. Liu, *Ionics*, 2020, **26**, 4985–4991.
- W. Li, D. Ye, S. Qiang and H. Hu, *Power Technol.*, 2023, **47**, 926–929.
- C. Zhang, W. Yang, B. Yao, L. Tang, J. Tang, J. Zhu, W. Yang, L. Zhou, Z. Pan and L. Fu, *J. Energy Storage*, 2024, **95**, 112557.
- P. Yang, X. Zhang, C. Zhang, S. Ma, X. Yang, Y. Xiong, Y. Xie, Y. Cao, Y. Cui and X. Liu, *J. Power Sources*, 2021, **511**, 230424.
- H. Sun, Y. Miao, G. Wang, X. Han, Y. Wang, Z. Zhang, C. Luo, X. Liu, C. Xu and H. Chen, *J. Energy Storage*, 2024, **76**, 109780.
- H. Sun, Y. Miao, G. Wang, X. Ren, E. Bao, X. Han, Y. Wang, X. Ma, C. Xu and H. Chen, *J. Energy Storage*, 2023, **72**, 108502.
- P. Masset and R. A. Guidotti, *J. Power Sources*, 2007, **164**, 397–414.
- F. Wang and X. Li, *ACS Omega*, 2018, **3**, 6006–6012.
- G. Liu, Preparation of Transition Metal Disulfides And Its Application in Thermal Batteries, Master thesis, China University of Mining and Technology, 2024.
- W. Cheng, P. Zhao, S. Yang, Y. Zhao and X. Zhan, *Power Sources Tech.*, 2016, **40**, 2192–2194.
- G. Liu, J. Jiang, X. Wang, C. Tang, Y. Cui and Q. Zhuang, *Mater. Lett.*, 2023, **330**, 133290.
- S. Xie, Y. Deng, J. Mei, Z. Yang, W.-M. Lau and H. Liu, *Composites, Part B*, 2016, **93**, 203–209.
- C. Jin, L. Fu, J. Zhu, W. Yang, D. Li and L. Zhou, *J. Mater. Chem. A*, 2018, **6**, 7123–7132.
- T. Yu, Z. Yu, Y. Cao, H. Liu, X. Liu, Y. Cui, C. Wang and Y. Cui, *Int. J. Electrochem. Sci.*, 2018, **13**, 7590–7597.
- Q. Tian, Z. Yu, Y. Wu and H. Liu, *J. Mater. Sci.: Mater. Electron.*, 2022, **33**, 13968–13976.
- X. Meng, H. Liu, S. Bi, C. Yang, S. Fan and L. Cao, *Electrochim. Acta*, 2023, **464**, 142879.
- H. Guo, L. Tang, Q. Tian, Y. Chu, B. Shi, X. Yin, H. Huo, X. Han, C. Yang and C. Wang, *ACS Appl. Mater.*, 2020, **12**, 50377–50387.
- P. Yang, Y. Cao, X. Zhang, Y. Xie, Y. Cui, S. Ma, K. Wei, Y. Wei, C. Wang and X. Li, *J. Power Sources*, 2022, **541**, 231717.
- H. Ning, Z. Liu, Y. Xie and H. Huang, *J. Electrochem. Soc.*, 2018, **165**, A1725–A1733.
- D. H. Jeon, *Energy Storage Mater.*, 2019, **18**, 139–147.

